



Contents lists available at ScienceDirect

Journal of Colloid and Interface Science

journal homepage: [www.elsevier.com/locate/jcis](http://www.elsevier.com/locate/jcis)

# Frequency-controlled electrophoretic mobility of a particle within a porous, hollow shell

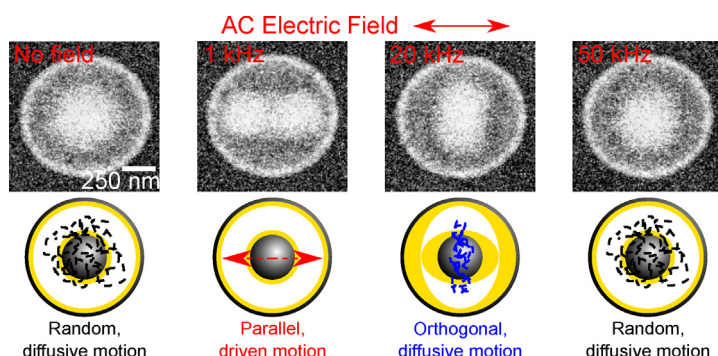
Tom A.J. Welling<sup>a,\*</sup>, Albert Grau-Carbonell<sup>a</sup>, Kanako Watanabe<sup>b</sup>, Daisuke Nagao<sup>b</sup>, Joost de Graaf<sup>c</sup>, Marijn A. van Huis<sup>a</sup>, Alfons van Blaaderen<sup>a,\*</sup>

<sup>a</sup>Soft Condensed Matter, Debye Institute for Nanomaterials Science, Utrecht University, Princetonplein 1, 3584 CC Utrecht, the Netherlands

<sup>b</sup>Department of Chemical Engineering, Tohoku University, 6-6-07 Aoba, Aramaki-aza, Aoba-ku, Sendai 980-8579, Japan

<sup>c</sup>Institute for Theoretical Physics, Center for Extreme Matter and Emergent Phenomena, Utrecht University, Princetonplein 5, 3584 CC Utrecht, the Netherlands

## GRAPHICAL ABSTRACT



## ARTICLE INFO

### Article history:

Received 2 April 2022

Revised 7 July 2022

Accepted 15 July 2022

Available online 20 July 2022

### Keywords:

Dynamic electrophoresis

Yolk-shell

Rattle-type particle

Hollow particles

Liquid phase electron microscopy

Electric field effects

Electrostatic interactions

## ABSTRACT

The unique properties of yolk-shell or rattle-type particles make them promising candidates for applications ranging from switchable photonic crystals, to catalysts, to sensors. To realize many of these applications it is important to gain control over the dynamics of the core particle independently of the shell. **Hypothesis:** The core particle may be manipulated by an AC electric field with rich frequency-dependent behavior.

**Experiments:** Here, we explore the frequency-dependent dynamic electrophoretic mobility of a charged core particle within a charged, porous shell in AC electric fields both experimentally using liquid-phase electron microscopy and numerically via the finite-element method. These calculations solve the Poisson-Nernst-Planck-Stokes equations, where the core particle moves according to the hydrodynamic and electric forces acting on it.

**Findings:** In experiments the core exhibited three frequency-dependent regimes of field-driven motion: (i) parallel to the field, (ii) diffusive in a plane orthogonal to the field, and (iii) unbiased random motion. The transitions between the three observed regimes can be explained by the level of matching between the time required to establish ionic gradients in the shell and the period of the AC field. We further investigated the effect of shell porosity, ionic strength, and inner-shell radius. The former strongly impacted

**Abbreviations:** LP-EM, liquid phase electron microscopy; (S) TEM, (scanning) transmission electron microscopy; EDL, electric double layer; AC, alternating current.

\* Corresponding authors.

E-mail addresses: [T.A.J.Welling@uu.nl](mailto:T.A.J.Welling@uu.nl) (T.A.J. Welling), [A.vanBlaaderen@uu.nl](mailto:A.vanBlaaderen@uu.nl) (A. van Blaaderen).

<https://doi.org/10.1016/j.jcis.2022.07.091>

0021-9797/© 2022 The Author(s). Published by Elsevier Inc.

This is an open access article under the CC BY license (<http://creativecommons.org/licenses/by/4.0/>).

the core's behavior by attenuating the field inside the shell. Our results provide physical understanding on how the behavior of yolk-shell particles may be tuned, thereby enhancing their potential for use as building blocks for switchable photonic crystals.

© 2022 The Author(s). Published by Elsevier Inc. This is an open access article under the CC BY license (<http://creativecommons.org/licenses/by/4.0/>).

## 1. Introduction

Colloidal crystals composed of complex building blocks are promising materials for optical [1], electrical [2], and biomedical applications [3], amongst many others. Examples of optical applications include photonic crystals and structural colors based on colloids, which have received considerable interest over the past decade [4–16]. Soft, colloid-based materials consisting of building blocks with adjustable separation allow for effective tuning of their optical (and other) properties via external stimuli, such as temperature, ionic strength, and external fields, e.g., electric or magnetic fields. Such tunability has the potential to diversify the applications of colloidal crystals, and has been used to create chemical or biological sensors [17,18], displays [19,20], and structurally colored paints and inks [21,22]. Control over the spacing and often also the symmetry of colloidal crystals has been achieved by inclusion of thermosensitive polymers [23,24] combined with a change in temperature or the application of external electric and magnetic fields [25,26]. However, previously reported switchable colloidal systems required reconfiguration of the building blocks via external magnetic [27–29] or electric fields [30–33]. It is desirable to create photonic materials where the underlying structure – endowing it with mechanical properties – is not changed, but the optical properties can be varied.

Yolk-shell particles, also referred to as ‘rattle-type’ particles, consist of a mobile core particle within a hollow shell [34–38], i.e., the core particle can be manipulated independently of the shell. As such, yolk-shell particles are promising soft matter systems from which to assemble switchable colloidal systems that do not require a structural reconfiguration of the material. Indeed, it was previously shown that the shells can be assembled into a 2D lattice and that the position of the core particles within the structure can subsequently be controlled using an external magnetic field [35] or alternating current (AC) electric field [37]. The assembled structures of the yolk-shell particles in the work of Watanabe and coworkers [37] had a lattice constant comparable to the wavelength of visible light. If the outer shells of these particles are refractive index-matched with the solvent inside and outside these shells, while the cores are not index-matched, these structures should have uniquely switchable optical properties [39]. That is, without applying an external field, the positions of the core particles are randomized within the shell due to Brownian motion, which significantly broadens the Bragg peaks resulting from coherent scattering of the cores with respect to, e.g., the idealized shell-centered position. Electric or magnetic fields could be used to position dielectric or magnetic cores at better defined locations within their shells and thus sharpen the Bragg peaks.

In this study, we elaborate on the work of Watanabe and coworkers [37]. Here, we clarify how the positioning of a diffusive core particle within a porous shell is modified by applying an external driving AC electric field, using both liquid-phase electron microscopy (LP-EM) experiments and finite-element calculations. Recent liquid-phase electron microscopy results have shown that Brownian motion [40,41] and interactions of particles can be observed at sufficiently low electron dose rates, for which the effects of the electrons could be neglected [42]. This technique yields nanometer resolution [43] and we applied it here to gain

information at the single particle level while applying an external AC electric field. The influence of important parameters such as frequency, salt concentration, shell thickness and porosity, and inner shell diameter were systematically explored while keeping the properties of the core particles constant. Before we discuss the results of this study, we introduce the relevant physical parameters and methods used.

### 1.1. Yolk-shell particle electrokinetics

This section briefly summarizes the most relevant electrokinetic concepts to aid in the understanding of our experimental and computational results. Colloidal particles dispersed in a liquid acquire a surface charge, which attracts an excess of opposite charges in the liquid to form a diffuse electric double layer (EDL) around the particles. The Debye screening length  $\kappa^{-1}$  is the typical length scale for the EDL thickness. An external electric field applied to a suspended, charged colloid leads to motion, referred to as electrophoresis [44–48]. The associated electrophoretic mobility  $\mu$  is defined as the ratio between the particle's electrophoretic velocity  $\mathbf{U}$  and the electric-field strength  $|\mathbf{E}|$

$$\mu = \frac{|\mathbf{U}|}{|\mathbf{E}|}. \quad (1)$$

This depends on the zeta potential  $\zeta$  of the particle, which is defined as the electric potential at the slipping plane [49], where the liquid velocity and the particle velocity are the same. For hard spheres with low  $\zeta$ ,  $\mu$  is given by the well-known Smoluchowski [50] and Hückel [51] expressions, holding in the limits of  $\kappa a \gg 1$  and  $\kappa a \ll 1$ , respectively, where  $a$  is the particle radius.

When working with alternating current (AC) electric fields, in our yolk-shell geometry, there are four relevant time scales: (i) The Maxwell–Wagner electrolyte relaxation time governs the rate of change for the charge distribution in the EDL. For a non-conducting particle it is given by [52,53]

$$\tau_{\text{MW}} = \frac{1}{\kappa^2 D_{\text{eff}}}, \quad (2)$$

where  $D_{\text{eff}} = \frac{2D^+D^-}{D^++D^-}$  is the effective diffusivity of the ions in the solution, which follows from electroneutrality. (ii) Diffusion relaxation establishes electrolyte concentration changes throughout the shell, and has an associated time scale

$$\tau_D = \frac{a_{\text{shell}}^2}{D_{\text{eff}}}, \quad (3)$$

where  $a_{\text{shell}}$  is the inner shell radius. Fig. 1 shows experimental images of the geometry. We consider  $\tau_D$  to be the most critical to our work, as it controls in-shell electrolyte dynamics. This includes concentration polarization [52], by which the EDL compresses on one side of the particle and expands on the other. (iii) The time for ions to electrically migrate over the shell radius is given by

$$\tau_{e,i} = \frac{a_{\text{shell}}}{\mu_{i,\text{eff}} |\mathbf{E}|}, \quad (4)$$

where  $\mu_{i,\text{eff}} = \frac{2\mu_i^+ \mu_i^-}{\mu_i^+ + \mu_i^-}$  is the effective electrical mobility of the ions in the solution and  $\mu_{i,\pm} = \lambda_{\pm}/F$ , where  $\lambda$  is the molar ionic conductivity

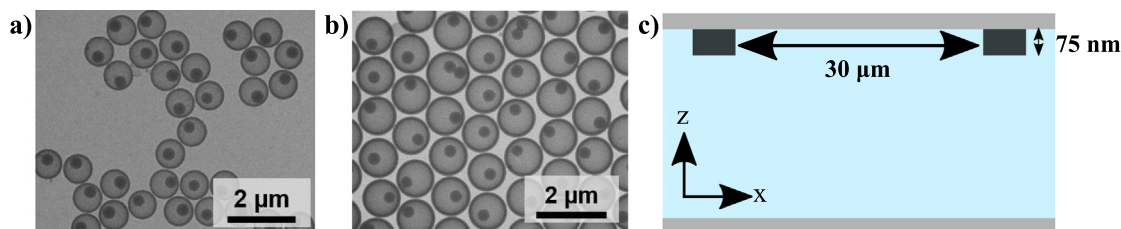


**Fig. 1.** a) Bright-field TEM image of yolk-shell particles consisting of a silica core particle ( $a_{\text{particle}} = 170\text{ nm}$ ) within a silica shell (inner radius  $a_{\text{shell}} = 370\text{ nm}$ , thickness  $t_{\text{shell}} = 40\text{ nm}$ ). b) Bright-field TEM image of yolk-shell particles consisting of a silica core particle ( $a_{\text{particle}} = 170\text{ nm}$ ) within a silica shell (inner diameter  $a_{\text{shell}} = 496\text{ nm}$ , thickness  $t_{\text{shell}} = 55\text{ nm}$ ). c) Schematic representation of the liquid-cell geometry in the experiments. The 75 nm thick platinum electrodes were on the top window of the liquid cell and were spaced 30 micron apart. The particles under investigation were located on the top window, approximately in the center between the two electrodes.

and  $F$  the Faraday constant. (iv) The time for the core particle to electrophoretically move over the shell radius, which is approximated as

$$\tau_{e,p} = \frac{a_{\text{shell}}}{\mu|\mathbf{E}|}. \quad (5)$$

In previous works, the dynamic electrophoresis of a free colloidal particle in bulk fluid was investigated both experimentally [54,55] and theoretically [44,56,57,53]. However, far fewer theoretical studies have been conducted into the electrophoretic mobility of charged spherical objects within a spherical cavity [58–66]. Of specific interest to our work are the calculations by Lee et al., who determined the electrophoretic mobility for a charged particle centered in a cavity (with equal charge and twice the size) [59]. These authors found that the electrophoretic mobility was enhanced compared to the mobility of a free particle when  $\kappa a \gg 1$ . This was also found in the calculations for dynamic electrophoresis by Tung and coworkers [61]. The increased mobility was attributed to the electric-field induced flow near the inner cavity wall, which contributes positively to the velocity of the particle inside the cavity. When  $\kappa a \ll 1$  the mobility of the core particle instead reduced due to the overlap of the double layers surrounding the particle and the inner cavity surface.

In our theoretical/numerical investigation, we drew inspiration from the above studies. However, there are two important differences: (i) our core particle is not stationary and (ii) ions can migrate through the porous shell. We account for the former in our numerical simulations by updating the position of the core at each time step and imposing its present velocity as the hydrodynamic boundary condition, as detailed in the Methods section.

## 2. Methods

For the synthesis of the yolk-shell particles the reader is referred to our previous collaborative work [37]. The particles used in this study are from the same batch as those in ref [37].

### 2.1. Liquid-phase electron microscopy experiments

In order to image the rattles in the electron microscope, we used a liquid-flow TEM holder with biasing capabilities (Protochips Poseidon Select, Protochips Inc., USA) and microchips with platinum electrodes. The microchips support 50 nm thick amorphous silicon nitride ( $\text{SiN}_x$ ) windows with lateral dimensions of 50 by  $200\text{ }\mu\text{m}^2$ . The spacer on one of the chips was 1000 nm in height. The two Si chips were glow-discharged (Cressington Power Unit 208) for 1 min prior to the experiment in order to make their surfaces more hydrophilic. The microchip with spacer was then placed in a dedicated holder. A  $1\text{ }\mu\text{L}$  droplet of the dispersion (particle volume fraction approximately 0.1 vol%) was dropcasted onto the microchip. The second microchip with the platinum electrodes

was placed on the bottom chip with the hydrophilic side facing the opposite chip. Two of the platinum electrodes were extending on the silicon nitride window of the chip and were spaced  $30\text{ }\mu\text{m}$  apart and are 75 nm thick. Some rattle particles stuck to the top window with their shells in between the electrodes, which allowed them to be imaged with the highest resolution and better defined electric field.

The liquid-phase scanning transmission electron microscopy (STEM) experiments were carried out using a transmission electron microscope (Tecnai 20F, Thermo Fischer Scientific), equipped with a field emission gun, and operating at 200 kV. The semi-convergence angle of the electron probe was 10 mrad. The annular dark-field (ADF) detector was used with a camera length of 120 mm. Image series were acquired with TEM imaging & analysis software (TIA). A frame recording time of 1 s was used. For a typical experiment the number of pixels was  $512 \times 512$ , with a pixel size of 8.8 nm. The screen current was measured to be 3.3 nA. These settings resulted in an electron dose rate of  $45\text{ e}^- \text{ nm}^{-2} \text{ s}^{-1}$ . Some slight deviations in those settings in different experiments did not lead to different behaviour of the core particles. For each frequency of the electric field an image series of 15 to 60 s was recorded with a frame time of 1 s. After applying an electric field of a certain frequency, the field was turned off for at least 20 s before an electric field with a different frequency was applied.

The electric field was applied via a Gamry Potentiostat 600+. It was connected in a two electrode configuration to the two electrodes on the electron-transparent window of the chip. A voltage of 3 V was applied which resulted in an electric field of  $100\text{ V mm}^{-1}$  (within 5% error, Supporting Figure S7) between the two electrodes which were spaced  $30\text{ }\mu\text{m}$  apart. The imaged particles were attached to the same window as the electrodes and were positioned approximately in the center between the two electrodes to avoid as best as possible electrode polarization effects. The AC electric field was applied for 15 – 60 seconds to observe the motion of the core particle at a particular frequency. The same aqueous LiCl solution that was already present in the liquid cell was flowed at  $2\text{ }\mu\text{L/min}$  to avoid bubble formation during electric field application and remove electro-chemical reaction products. Some experiments were performed without flow and the resulting motion of the core particle was observed to be unchanged. The salt concentration within the liquid-cell geometry was changed by flowing in a given aqueous LiCl solution for at least 15 min before any electric field experiments were performed. It was confirmed that the new salt concentration was present within the shell by observation of how close the particle could approach the shell [42].

### 2.2. Finite-element calculations

We performed finite-element calculations using COMSOL Multiphysics (V5.4). We used an axisymmetric calculation domain to reduce the computational overhead and complete calculations in

a reasonable time on a modern, high-performance workstation. Two separate calculations were performed. First we calculated the equilibrium EDLs in the yolk-shell geometry without an externally applied electric field, for the case that the core particle was situated in the middle of the yolk-shell geometry and remained stationary. Subsequently, a time-dependent study was performed to calculate the evolution of the ion distribution, fluid flow, and electric potential, as well as the position of the core particle in time. The fluid was assumed to be incompressible and its dynamics captured by the creeping flow form of the Navier–Stokes equations, that is, friction dominates inertia and the Reynolds number is much smaller than unity. Electromigration, convection, and diffusion of ionic species were accounted for using a combination of the Poisson equation and Nernst–Planck equation. The governing equations of the problem are then the following:

$$\nabla^2 \phi = -\frac{\rho_c}{\epsilon_0 \epsilon_r} = -\sum_{j=1}^2 \frac{e z_j n_j}{\epsilon_0 \epsilon_r} = \frac{e(n_- - n_+)}{\epsilon_0 \epsilon_r}, \quad (6)$$

$$\frac{\partial n_j}{\partial t} = -\nabla \cdot \left( -D_j \left( \nabla n_j + \frac{e n_j z_j}{k_B T} \nabla \phi \right) + n_j \mathbf{u} \right), \quad (7)$$

$$\nabla \cdot \mathbf{u} = 0, \quad (8)$$

$$\rho_{\text{fluid}} \frac{\partial \mathbf{u}}{\partial t} = -\nabla p + \eta \nabla^2 \mathbf{u} - \rho_c \nabla \phi. \quad (9)$$

In these equations  $\nabla^2$  is the Laplace operator,  $\phi$  is the electric potential,  $\rho_c$  is the space charge density,  $\epsilon_0$  is the permittivity of free space,  $\epsilon_r$  is the relative permittivity of the liquid,  $e$  is the elementary charge, and  $n_j$  is the number density of ionic species  $j$ . Furthermore,  $\nabla$  is the gradient operator,  $D_j$  is the diffusion coefficient of ionic species  $j$ ,  $\mathbf{u}$  is the velocity of the fluid and  $t$  is time, while  $\rho_{\text{fluid}}$  and  $\eta$  are the fluid density and viscosity, respectively, and  $p$  is the pressure. Note that we chose to limit the number of charged species to two, both of which are monovalent.

We assumed that the surface conductivities of the particle and shell were negligible. Furthermore, the dielectric constant of silica ( $\epsilon_r = 3.8$ ) is much smaller than that of water ( $\epsilon_r = 78.4$ ). Therefore, a constant surface charge density  $\sigma$  boundary condition on the surface of the core particle, as well as on the inner and outer surface of the shell was used.

We assumed a no-slip boundary condition on the surface of the core particle as well as the inner and outer surface of the shell. The fluid velocity on the particle's surface was the same as the velocity of the particle. This leads to the boundary conditions:

$$\mathbf{u} = \mathbf{U}, \quad r = a_{\text{particle}}, \quad (10)$$

$$\mathbf{u} = 0, \quad r = a_{\text{shell}}, \quad (11)$$

$$\mathbf{u} = 0, \quad r = a_{\text{shell}} + t_{\text{shell}}, \quad (12)$$

where  $\mathbf{U}$  is the velocity of the particle,  $a_{\text{particle}}$  the particle radius,  $a_{\text{shell}}$  the inner shell radius, and  $t_{\text{shell}}$  the shell thickness. Furthermore, the surface of the particle was impermeable to ions, so that

$$(\mathbf{f}_j - n_j \mathbf{u}) \cdot \hat{\mathbf{n}} = 0, \quad r = a_{\text{particle}}, \quad (13)$$

where  $\mathbf{f}_j = -D_j(\nabla n_j + (e n_j z_j / k_B T) \nabla \phi) + n_j \mathbf{u}$  is the concentration flux of ionic species  $j$  and  $\hat{\mathbf{n}}$  is the unit normal to the particle surface. The shell was not impermeable to ionic species in the experiments. In our model the shell has a porosity  $\Phi_p$  and it is therefore possible for ions to diffuse through. The diffusivity of ion species  $j$  through the shell  $D_{sj}$  is related to the bulk diffusivity of that ion species  $D_j$  via

$$D_{sj} = \Phi_p D_j. \quad (14)$$

Furthermore, the dielectric constant of the shell  $\epsilon_{r,s}$  is related to the dielectric constant of water  $\epsilon_{r,\text{water}}$  and that of silica  $\epsilon_{r,\text{silica}}$  as

$$\epsilon_{r,s} = \Phi_p \epsilon_{r,\text{water}} + (1 - \Phi_p) \epsilon_{r,\text{silica}}. \quad (15)$$

The electrophoretic mobility of the particle  $\mu$  can be expressed as

$$\mu = \mu_R + i\mu_I = \frac{\mathbf{U}}{\mathbf{E}}, \quad (16)$$

where  $\mathbf{U} = U_R + iU_I$  is the complex particle velocity and  $\mathbf{E} = E_z e^{-i\omega t}$  is the external electric field. The velocity of the particle is determined by the electric force and the hydrodynamic drag force acting on it via Newton's second law of motion [53]

$$\mathbf{F}_e + \mathbf{F}_h = \frac{4}{3} \pi a_{\text{particle}}^3 (\rho_{\text{particle}} - \rho_{\text{fluid}}) \frac{d\mathbf{U}}{dt}, \quad (17)$$

where  $\rho_{\text{particle}}$  is the density of the particle. Immediately after applying an electric field, a colloidal particle starts an accelerated motion [52]. The viscous friction leads to a constant velocity after a time given by the time scale [52,53]

$$\tau_H = \frac{\rho_{\text{fluid}} a_{\text{particle}}^2}{2\eta}. \quad (18)$$

This time scale for our particle of  $a_{\text{particle}} = 170\text{nm}$  in water is approximately 14ns (Supporting Figure S15). We stress that the acceleration term is negligible after this initial acceleration period and has a negligible influence on the overall dynamics, as expected for a particle in a fluid at low Reynolds number. Often this is accounted for in modeling by setting the right-hand side of Eq. 17 to zero, i.e., neglecting the inertia completely, and solving directly for the particle velocity from the hydrodynamic friction. We chose not to make this reduction here, as this would have complicated our numerical solving strategy.

The electric force and hydrodynamic drag force were obtained by integrating the electric and hydrodynamic stress tensor over the surface of the particle, respectively.

$$\mathbf{F}_h = \oint_S \mathbf{T} dS \quad (19)$$

$$\mathbf{F}_e = \oint_S \mathbf{M} dS. \quad (20)$$

As water was the suspension medium and Stöber-like silica was the material for the shell and core particles in this study, we used the following material parameters: the relative permittivity of the water  $\epsilon_r = 78.4$ , the relative permittivity of silica  $\epsilon_r = 3.8$ , the viscosity of the fluid  $\eta = 1\text{mPas}$ , the density of the fluid  $\rho_{\text{fluid}} = 1\text{gcm}^{-3}$ , the density of the core particle  $\rho_{\text{particle}} = 2\text{gcm}^{-3}$ , the temperature  $T = 293.15\text{K}$  and the ionic diffusivities [67]  $D_{Li} = 1.022 \cdot 10^{-9}\text{m}^2\text{s}^{-1}$  and  $D_{Cl} = 2.037 \cdot 10^{-9}\text{m}^2\text{s}^{-1}$ .

### 3. Results and discussion

#### 3.1. Frequency-dependent mobility of the core particle

Liquid-phase electron microscopy experiments were performed to capture the frequency-dependent motion of negatively charged silica core particles within porous, negatively charged silica shells (Fig. 1a–b). The particles were synthesized as described in the work of Watanabe and coworkers [37]. In short, particles were loaded between two microchips within a commercial liquid-cell holder. The top microchip contained 75nm thick platinum electrodes spaced 30μm apart that were used to apply an electric field (Fig. 1c). We mostly imaged the yolk-shell particles that were in the middle between the electrodes with the shell attached to the top chip, so that a uniform electric field could be applied with minimal effects of electrode polarization (Supporting Figure S7).

First, the motion of a core particle (radius  $a_{\text{particle}} = 170\text{nm}$ ) within a hollow silica shell (inner radius  $a_{\text{shell}} = 370\text{nm}$ , thickness



$t_{\text{shell}} = 40 \text{ nm}$ ) was observed in an aqueous solution of  $2.00 \text{ mM}$  LiCl ( $\kappa a_{\text{particle}} \approx 26$ ) using liquid-phase STEM. The electron dose rate was  $45 \text{ e}^- \text{ nm}^{-2} \text{ s}^{-1}$ . Fig. 2 shows the projected area that the core particle explored within 50 s of recording time, when an AC electric field of the indicated frequency was applied at an electric-field strength of  $100 \text{ V mm}^{-1}$ . Three frequency-dependent regimes were observed, which is best appreciated in Supporting Movie 1. When no field was applied, the cores were seen to explore a certain part of the shell geometry *via* thermal fluctuations constrained by the equilibrium double layers of the core and the shell. When a low frequency electric field of  $2 \text{ kHz}$  or lower was applied, the motion of the core was driven by the field in a direction parallel to the electric field. That is, the particle was moved from one side of the shell to the other, while the Brownian displacements were suppressed. From  $3$  to  $7 \text{ kHz}$  the mostly field-driven core motion gradually changed to diffusive motion orthogonal to the electric field. Supporting Movie 1 shows that in the regime from  $3$  to  $7 \text{ kHz}$  there was still a significant displacement of the core in the parallel direction driven by the electric field. However, with increasing frequency the displacement in the parallel direction decreased in magnitude from around  $350 \text{ nm}$  for  $1$ – $2 \text{ kHz}$  to  $120 \text{ nm}$  for  $7 \text{ kHz}$ , and further reducing to  $40 \text{ nm}$  at  $20 \text{ kHz}$ . The motion was always centered around the middle of the shell. It was also observed that the diffusive motion in the orthogonal direction gradually increased from  $3$  to  $7 \text{ kHz}$ . As mentioned, the motion orthogonal to the electric field was not driven by the electric field, as was the case for the parallel motion. Instead the motion was diffusive-like, which is most readily appreciated from Supporting Movie 1. Apparently, the electric field prevented the core to move away from the center in the direction parallel to the field, which hints at changed ionic double layer interactions due to the electric field. At even higher frequencies, greater than  $40 \text{ kHz}$ , the core showed diffusive behaviour indistinguishable from when no elec-

tric field was applied. The experiments thus revealed several regimes for both directly driven and more diffusive displacements of the core particles in different directions.

Finite-element calculations were performed using COMSOL MultiPhysics to provide understanding of the experimental observations. Full details are given in the Methods section and Supporting Information. In short, we solved the coupled equations for fluid dynamics, ionic transport, and electric potential within the yolk-shell geometry. First a calculation for which the colloidal particle did not move was performed to acquire the equilibrium EDLs in the yolk-shell geometry, without an electric field for the case where the core particle was situated in the middle of the yolk-shell geometry. Subsequently, a time-dependent study was performed to calculate the evolution of the ion distribution, fluid flow, and electric potential, and the position of the core particle in time (as calculated from the electric and hydrodynamic forces acting on the particle) during the application of three AC electric field cycles of various frequencies. Because the particle moved during the time-dependent study, the electrophoretic velocity is dependent on both time and position.

In the calculations, for an ionic strength of  $I = 2 \text{ mM}$  we used constant surface charge density boundary conditions ( $\sigma = -6.3 \text{ mC m}^{-2}$ ) for the core and the shell, which resulted in a surface potential of  $-50 \text{ mV}$  for the core and  $-40 \text{ mV}$  for the shell. These were roughly in line with measurements of the zeta potential (Supporting Information) and literature values for the zeta potential of Stöber silica particles [68]. We should mention that there is an inherent difficulty in measuring the zeta potential of core particles inside shells, as well as the zeta potential of the inner surface of a shells. This is because common techniques such as electrophoretic light scattering cannot easily be used.

Fig. 3a shows the evolution of the particle position for three cycles of the electric field for different frequencies when a shell porosity of  $10\%$  is assumed. In these calculations, the porosity of

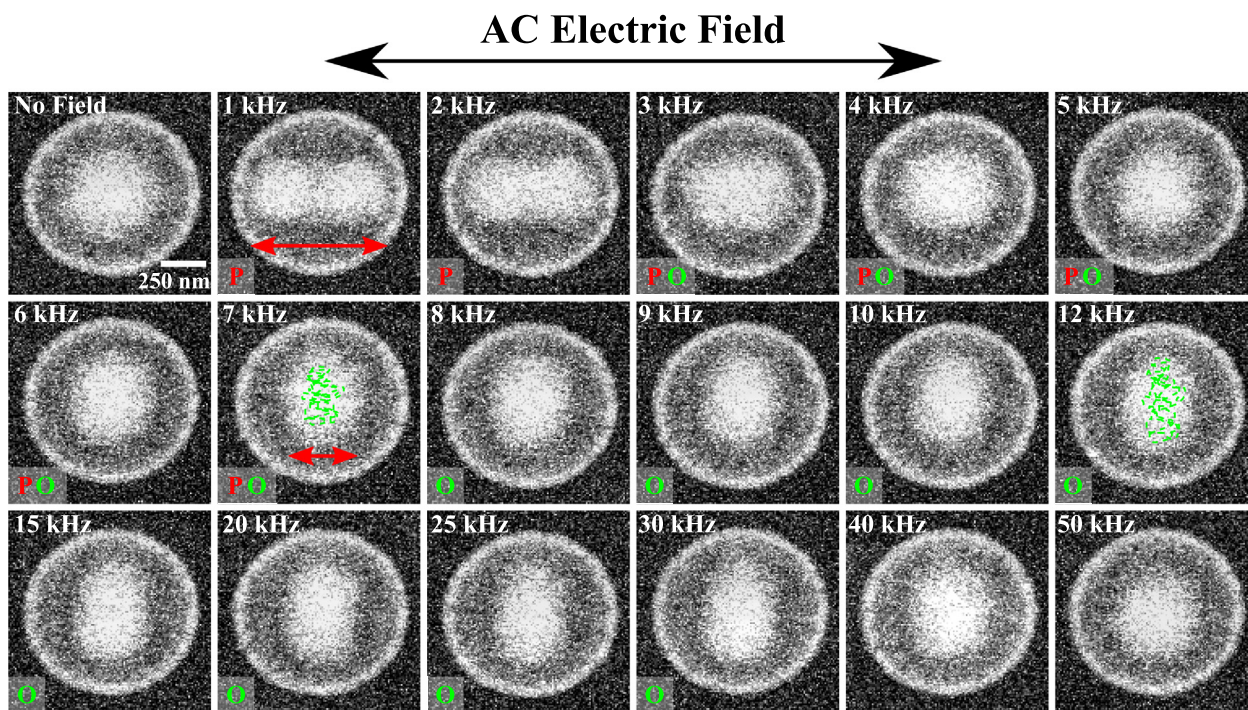


**Fig. 2.** Frequency-dependent mobility of a core particle ( $a_{\text{particle}} = 170 \text{ nm}$ ) within a shell (inner radius  $a_{\text{shell}} = 370 \text{ nm}$ , thickness  $t_{\text{shell}} = 40 \text{ nm}$ ) under application of a  $100 \text{ V mm}^{-1}$  AC electric field in aqueous solution of  $2.00 \text{ mM}$  LiCl. The electron dose rate was  $45 \text{ e}^- \text{ nm}^{-2} \text{ s}^{-1}$ . The bright area within the shell indicates the part of the cavity that was explored by the core over a 50 s period as observed in Supporting Movie 1. The images here are cropped from the total movie that was 512 by 512 pixels, with a pixel size of  $8.75 \text{ nm}$ . The frame time was  $1 \text{ s}$ . At lower frequencies the core was driven by and parallel (P) to the electric field as indicated by the red arrow. At intermediate frequencies ( $3$ – $30 \text{ kHz}$ ) the core diffused orthogonal (O) to the electric field as indicated by the light green dashed paths. At higher frequencies ( $> 40 \text{ kHz}$ ), there was no significant influence of the electric field.

the shell  $\Phi_p$  is assumed to determine the diffusivity of ion species  $j$  through the shell  $D_{sj}$  compared to the bulk diffusivity of ions  $D_j$  as

$$D_{sj} = \Phi_p D_j. \quad (21)$$

While experimentally the actual diffusion coefficient of ions through the shell is unknown, Eq. 21 allows us to investigate how the porosity of the shell influences our system. For the highest frequency fields, the variation of the field was still sufficiently slow for

the particle to track the electric field [53]. However, at these frequencies, the electric field switches so fast that the particle moves only a few nanometer, before the electric field changes direction. As such, no interesting behaviour is observed at the highest frequencies (50 – 100 kHz).

At 5 kHz, the particle did not return exactly to the same position after a full electric field cycle was completed. Instead, the particle, while showing sinusoidal behaviour (Fig. 3a), also on average moves back to the middle of the yolk-shell geometry. This is likely

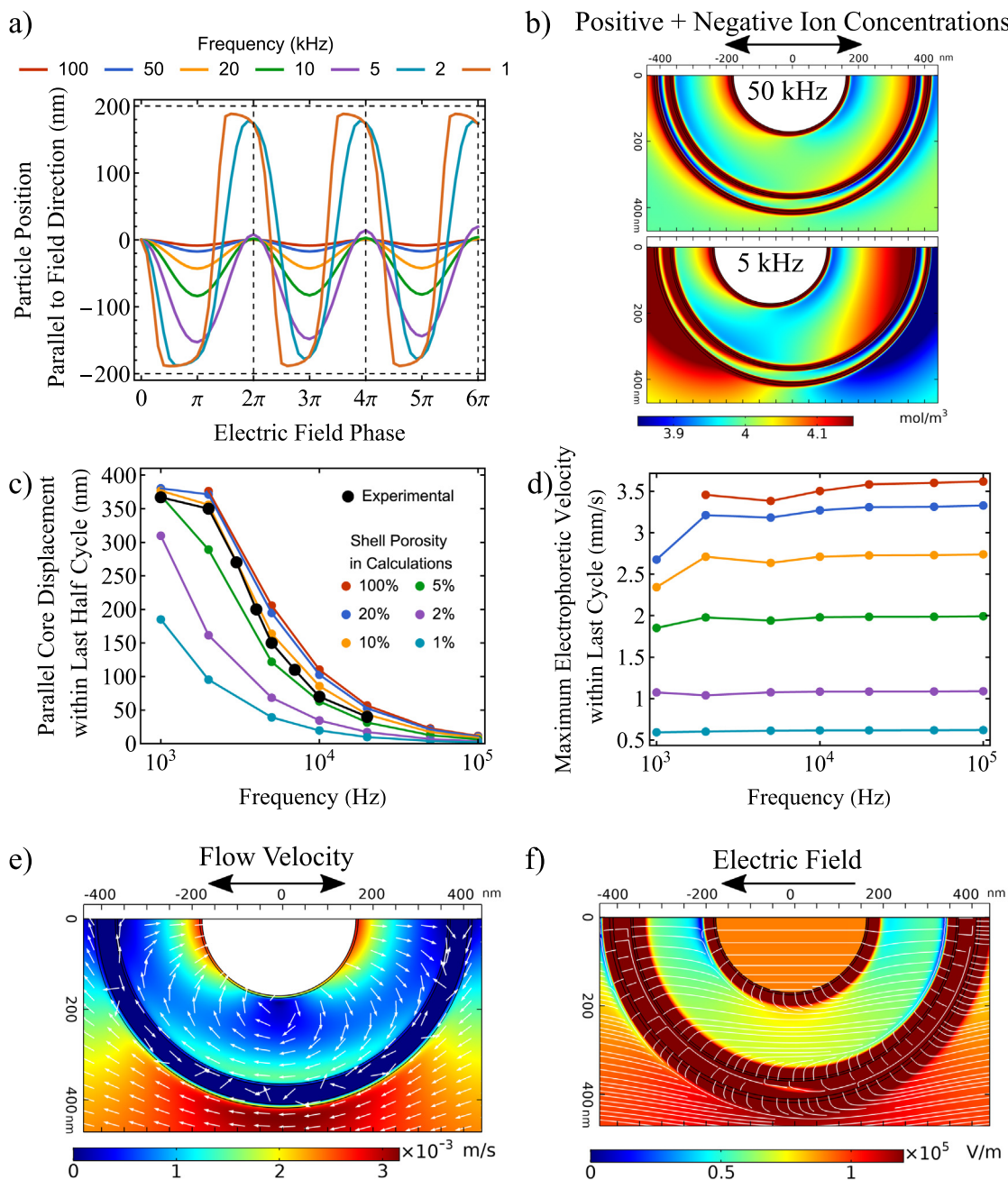


**Fig. 3.** Calculated frequency-dependent mobility of a core particle ( $a_{\text{particle}} = 170\text{ nm}$ , surface potential  $\phi = -50\text{ mV}$ ) within a shell ( $a_{\text{shell}} = 370\text{ nm}$ ,  $t_{\text{shell}} = 40\text{ nm}$ , surface potential  $\phi = -40\text{ mV}$ ) during  $100\text{ V mm}^{-1}$  AC electric field application in aqueous solution of  $2\text{ mM}$  ionic strength. a) The particle position in time during 3 cycles of the electric field for different frequencies. The porosity of the shell was taken to be 10%. The horizontal dashed lines show the position for which the particle would touch the inner shell wall. b) Concentration of positive plus negative ions after 2.75 cycles of the electric field ( $5.5\pi$ ) at 50 and 5 kHz. The double-headed arrow indicates the electric field direction. c) Parallel displacement of the core particle within the last half cycle of the electric field as function of frequency for different shell porosities. A porosity of the shell of 10% results in a core mobility that very closely resembles the experimental mobility of the core particles. d) The maximum electrophoretic velocity of the core particle as function of frequency for different shell porosities. e-f) Flow velocity and electric field after 2.75 cycles of the electric field ( $5.5\pi$ ) at 50 kHz. The single-headed arrow in f corresponds to the electric field direction at that point in time.



due to concentration polarization, which disturbs the equilibrium ion concentrations within the yolk-shell geometry (Fig. 3b). The time needed for this phenomenon to occur within our system is related to the time scale associated with diffusive motion of ions over the shell radius  $\tau_D \approx 1.0 \cdot 10^{-4}$  s, which corresponds well with a frequency of 5 kHz. The time scale associated with electrophoresis of ions (molar ion conductivities [69] 38.6 and 76.4  $\Omega^{-1}$  for  $\text{Li}^+$  and  $\text{Cl}^-$ , respectively) over the shell radius for a field strength of 100 V  $\text{mm}^{-1}$ ,  $\tau_{e,i} \approx 6.2 \cdot 10^{-5}$  s, also agrees well with the frequencies at which we see significant disturbances in the equilibrium ion concentrations. Fig. 3b indeed shows that the changes in the ion concentrations within the shell are more significant for 5 kHz than for 50 kHz, even though changes already occur at 50 kHz. We revisit the trend of the particle migrating back to the middle of the yolk-shell geometry at 5 kHz in more detail later.

For 1 kHz the particle has enough time before the electric field changes direction to closely approach the inner shell wall. At that point the electric double layers of the particle and the inner shell wall overlapped significantly, which did not allow the particle to move further. The particle trajectory at 1 kHz was therefore not symmetric (Fig. 3a), as the particle nearly arrested close to the shell, until the field reversed direction. This also explains why the core particle attained a smaller maximum speed for 1 kHz than for higher values of the frequency (Fig. 3d) as the particle was arrested near the particle shell before the electric field reached its maximum strength. The particle moving from one side of the shell to the other for a frequency of 2 kHz or lower corresponds relatively well to the time scale for electrophoresis of a 170 nm free particle over the shell radius  $\tau_{e,p} \approx 1.1 \cdot 10^{-4}$  s. Furthermore, it agrees well with the experimental results that showed the particle moving from one side of the shell to the other for frequencies of 2 kHz or lower (Fig. 2).

Fig. 3c-d shows that the porosity of the shell has a large influence on the mobility of the core particle within. The porosity of the shell influences the mobility in the calculations in two ways. First, the porosity determines the dielectric constant of the shell by a weighted average between the dielectric constant of water ( $\epsilon_r = 78.4$ ) and silica ( $\epsilon_r = 3.8$ ). Second, it determines how fast ions are able to migrate through the shell (Eq. 21). The time scale for ion diffusion through the shell is

$$\tau_s = \frac{t_{\text{shell}}^2}{D_{s,\text{eff}}}, \quad (22)$$

where  $t_{\text{shell}}$  is the thickness of the shell and  $D_{s,\text{eff}}$  is the effective ion diffusion coefficient through the shell. For a 40 nm thick shell with 100% porosity, and therefore  $D_{s,\text{eff}} = D_{\text{eff}}$ ,  $\tau_s \approx 10^{-6}$  s. For a porosity of 1% the time scale for ions to migrate through the shell becomes  $\tau_s \approx 10^{-4}$  s, which is similar to the diffusion relaxation time  $\tau_D$ , which we argued in the introduction to control the dynamics of the core. It was found that porosities of 10% and lower can lead to a significantly reduced electric field within the yolk-shell geometry (Supporting Figure S9), which can therefore lead to a reduced electrophoretic velocity of the core.

For now, we focus on the calculations for a shell where a porosity of 10% is assumed, which is in best agreement with the experiments (Fig. 3c). From Fig. 3c it follows that a change in the porosity of the shell leads to a large difference in the mobility of the particle. However, a porosity of 5 to 100% in the calculations can all explain the experiments relatively well. Later we study the mobility of the core particles in shells with different thickness/porosities in more detail. The drop in electric-field strength within the yolk-shell geometry is predominantly caused by the dielectric constant of the shell at high porosities ( $> 10\%$ ) (Figs. 3f and S8). For a porosity of 10%, the electric-field strength within

the shell is approximately 60 V  $\text{mm}^{-1}$ . Using Smoluchowski's equation we calculated that a free particle with a zeta potential of  $-50$  mV in a 60 V  $\text{mm}^{-1}$  electric field would have an electrophoretic velocity of 2.1  $\text{mm s}^{-1}$ , which is significantly lower than that of the same particle in the same electric field in the charged shell (2.7  $\text{mm s}^{-1}$ ). Such a high mobility of a charged particle in a charged cavity was observed earlier in theoretical studies [59,61,66]. The particle within the charged shell can move faster than a free particle because the flow coming from the EDL originating from the inner shell wall contributes positively to the particle mobility, as shown in Fig. 3e. Additionally, Figure S11 shows a positive relationship between particle displacement and inner shell surface charge. As such, competing effects of the shell porosity and shell EDL contribute to the mobility of the particle. The shell porosity and dielectric constant determine the electric-field strength inside the cavity, where the EDL originating from the inner shell wall influences the mobility of the particle by induced flows.

To experimentally test whether the diffusion of ions through the shell indeed influenced the observed driven and diffusive core motion patterns, we changed the porosity of the original sample by both etching the shell further and overgrowing the shell with an extra porous silica layer. This is expected to make the shell easier or harder for the ions to diffuse through, respectively. The etched shell showed larger pores within the shell compared to the original sample, while the thicker shell was increased in thickness compared to the shell of the original sample, from 40 nm to 110 nm thickness, as can be appreciated from Fig. 4. The extra layer of the shell that was grown should also be less porous as it was not subjected to any etching steps. Fig. 4 shows the projected area that the core explored during the application of the electric field at a certain frequency. The sample with extra etched shells showed similar behaviour as the original sample (Fig. 2), except that the orthogonal diffusive motion from the original sample was not observed, and the core was instead mostly confined to the center of the etched shell. The parallel mobility at lower frequencies was the same as for the original sample. For the thicker shell, the fully parallel motion was only observed when an external electric field of a frequency of 50 Hz was applied. The shift to lower frequencies is in qualitative agreement with the finite-element calculations (Fig. 3c). It is likely caused by the lower electric-field strength within the shell geometry, possibly also combined with less ions being able to be transported through the shells, which reduced the electrophoretic velocity of the particle within. At higher frequencies no significant orthogonal/suppressed motion was found for the overgrown shell, which is unlike the original sample and the sample with the etched shell. This result can also be explained by the low electric-field strength within the shell geometry (Supporting Figure S8). When the field inside the yolk-shell geometry is not sufficiently high, the ion concentrations are not significantly disturbed. This experimental evidence shows that the shell thickness and porosity influences the electrophoretic mobility of the core particle within significantly.

### 3.2. Origin of the suppression of parallel motion of the core particles

Next we aim to understand the diffusive orthogonal motion of core particles at frequencies around 5–20 kHz for the original sample (Fig. 2). We performed finite-element calculations for which the core particle was initially placed 100 nm off-center in the direction parallel to the electric field. If the parallel motion is suppressed like in the experiments, we expect the core particle to return to the center of the rattle geometry when the AC electric field is applied. Fig. 5 shows the evolution of the particle position when we placed the particle 100 nm off-center in the direction parallel to the electric field. For all frequencies under consideration the particle moved towards the center. However this effect was lar-

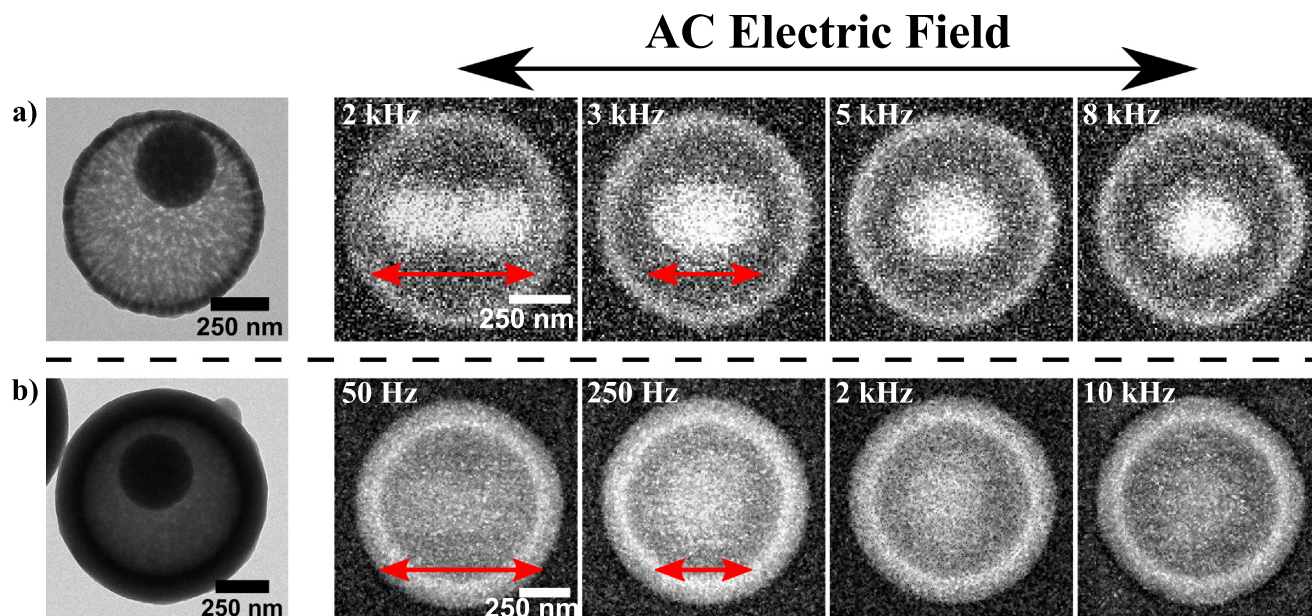


**Fig. 4.** Frequency-dependent mobility of a core particle ( $a_{\text{particle}} = 170 \text{ nm}$ ) within a more porous ( $t_{\text{shell}} = 40 \text{ nm}$ ) (a) or thick ( $t_{\text{shell}} = 110 \text{ nm}$ ) (b) shell under application of a  $100 \text{ V mm}^{-1}$  AC electric field in aqueous solution of  $2.00 \text{ mM LiCl}$ . For the etched shell images, the electron dose rate was  $148 \text{ e}^- \text{ nm}^{-2} \text{ s}^{-1}$ . The pixel size was  $8.8 \text{ nm}$ , the frame time was  $1 \text{ s}$  and the total frame was  $256$  by  $256$  pixels. For the thick shell images, the electron dose rate was  $156 \text{ e}^- \text{ nm}^{-2} \text{ s}^{-1}$ . The pixel size was  $5.8 \text{ nm}$ , the frame time was  $1 \text{ s}$  and the total frame was  $512$  by  $512$  pixels. The images shown are zoom-ins of the original movies. The bright area within the shell indicates the part of the cavity that was explored by the core over a  $20 \text{ s}$  period as observed in Supporting Movies 2–3. The red arrow indicates that the particle motion is driven by the electric field.

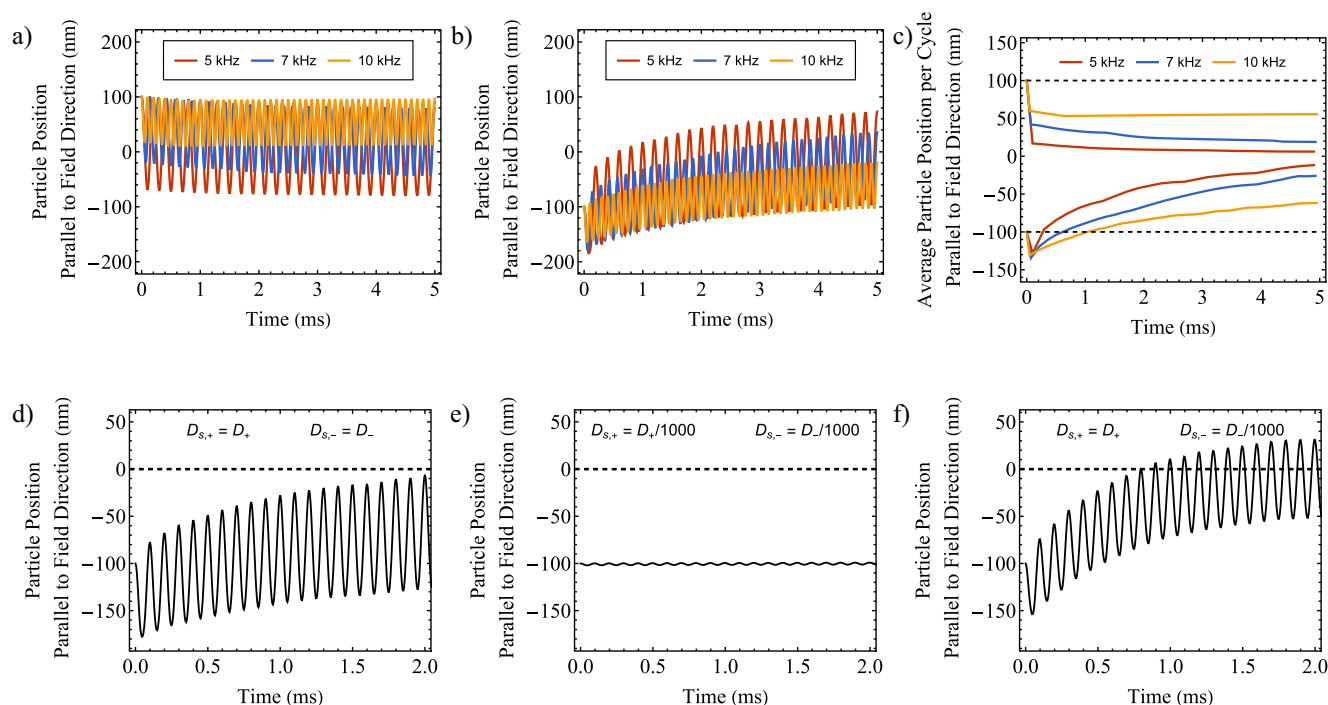


**Fig. 5.** Particle response to the electric field from finite-element calculations at an ionic strength of  $2 \text{ mM}$  and a shell porosity of  $10\%$  when the particle was initially placed off-center in the direction parallel to the electric field. a–c) The influence of the frequency on the core relaxing back to the middle of the shell when initially placed off-center. The shell was given a porosity of  $10\%$  ( $\epsilon_r = 11.3$ ,  $D_{s,+} = D_+/10$ ,  $D_{s,-} = D_-/10$ ). The particle was placed at  $+100$  and  $-100 \text{ nm}$  from the center in a and b, respectively. c) The average position per cycle of the core particle, for the particle starting at  $+100$  and  $-100 \text{ nm}$  from the center. The dashed lines show the particle position when there was no electric field applied (and without Brownian motion). They indicate that equilibrium double layers do not meaningfully push the particle back to the middle in the time scale under investigation. d–f) The influence of limiting the diffusion coefficient of ions migrating through the shell. The frequency is  $10 \text{ kHz}$  and the dielectric constant of the shell is  $\epsilon_r = 78.4$ . d) Both ions diffuse through the shell with the same diffusion coefficient as in the bulk. e) Both ions have difficulty diffusing through the shells, because their diffusion coefficient through the shell is a factor  $1000$  lower than in the bulk. f) The positive ions diffuse through the shell with their bulk diffusion coefficient, while the diffusion coefficient of the negative ions through the shell is a factor  $1000$  lower than in the bulk. The parameters such as particle size, surface potentials, and electric field strength for a–f were the same as in Fig. 3.



gest for the lowest frequency, 5 kHz. The time scale for ion concentrations to be established within the yolk-shell geometry is  $\tau_D \approx 1.0 \cdot 10^{-4}$  s. This time scale matches well with those in the frequency range for which the particle motion in the direction parallel to the electric field is suppressed. At these frequencies the ions have enough time to compress/extend the double layers within the yolk-shell geometry [52]. From Fig. 5 we observe that the particle moves back to the middle of the shell more quickly when it is initially placed at +100 nm from the center, compared to when it is initially placed at –100 nm. This is because the AC electric field first drives the particle in the negative direction, before it directs the particle in the positive direction later in the electric field cycle. As such, when the particle starts at +100 nm the particle is pushed towards the middle initially.

Next we investigated whether the ability of ions to migrate through the shell influences the inhibition of parallel core motion at 10 kHz. In Fig. 5d–f, d–f, the core particle was initially placed off-center (–100 nm) and a transient, time-dependent calculation was performed. The shell had a dielectric constant of 78.4, and the diffusion coefficients of the ions through the shell were changed in each subfigure. We found that when the diffusion coefficient of both ions through the shell was severely suppressed (Fig. 5e) the particle did not relax back to the middle of the shell due to the electric field. This is likely why no suppression of parallel motion was observed for the yolk-shell particles with a thicker, less porous silica shell (Fig. 4b). Furthermore, we performed a transient calculation for which only the diffusion coefficient of the negative ion through the shell was lowered. This choice is motivated by the negative charge of the silica shell and the nanometric pore size of the material. The Debye screening length in 2 mM LiCl (aq) is 6.8 nm, which is larger than the width of the pores. Therefore, the pores are filled with counterions [70], which leads to a negative Donnan potential that tends to exclude co-ions [71]. A situation where the diffusion coefficient of negative ions through the shell was lowered by a factor 1000, while the positive ion diffusivity through the shell was the same as the bulk diffusivity, is shown in Fig. 5f. We note here that ions moving through the shell with a diffusion coefficient 1000 times smaller than in the bulk, still means that ions easily migrate through the shell on the time scale of seconds to minutes. The suppression of negative ion migration through the shell actually stimulates the relaxation of the core particle back to the middle of the shell, compared to when both ions easily migrate through the shell (Fig. 5d). A reason for this could be that the double layers within the shell geometry are more easily extended when co-ions are unable to migrate through the shell to compensate for the electric-field induced gradients. This effect results in a larger suppression of the parallel motion of the core when co-ion migration through the shell is hindered. These calculations corroborate the experimentally observed results that ion migration through the shells significantly alters the electrokinetic phenomena within the shell geometry (Fig. 4).

A major difference between our numerical calculations and the experiment is that Brownian motion is also present in the latter. To substantiate our claims regarding the mechanisms by which orthogonal motion is achieved, we consider the effects of Brownian motion. The applied field causes the particle to move to the center of the shell in approximately 2 ms, see Fig. 5. In contrast, a free particle with a radius of 170 nm moves on average 50 nm in one dimension in 2 ms via Brownian motion, which is similar to the distance over which the particle is pushed back by the effects of the electric field. This is an upper bound to the diffusion, as the diffusion of a particle within a shell is reduced compared to that of a free particle [42,72,73]. We conclude that the effect of the electric field is strong enough to indeed limit diffusive motion of the core particles in the direction parallel to the electric field. Due to Brownian motion, the particles in the experiments still move orthogonally to the electric field, while they are hindered from moving parallel to the electric field. As such, orthogonal motion is observed in the experiments.

### 3.3. Influence of ionic strength

Experimentally, three different salt concentrations were used to investigate the influence of the thickness of the equilibrium double layers on the frequency dependence on the core particle motion (Supporting Movies 1, 4, and 5). Fig. 6 shows the projected area within the shell that was explored by the core particle at various frequencies of the applied electric field for ionic strengths of 0.200, 2.00, and 25.0 mM ( $\kappa a_{\text{particle}} \approx 8, 26, \text{ and } 88$ ). These concentrations were chosen as the equilibrium EDLs for these concentrations either confine the core particles to the middle of the shell (for 0.200 mM) or allow the core particles to approach the inner shell wall extremely closely (25.0 mM) [42]. When turning on the AC electric field, we observed similar motion for the core particles for all LiCl concentrations. The core particles exhibited parallel, driven motion at low frequencies ( $< 3$  kHz), orthogonal, diffusive motion at intermediate frequencies (3–40 kHz) and random motion at high frequencies ( $> 40$  kHz). An almost identical frequency-dependent motion was observed for all ionic strengths, with only slight differences. This strengthens our previous argument that ion concentrations within the whole shell geometry, rather than only those in the initial double layers, determine the core mobility regimes.

We will now discuss why parallel motion was observed for the core particles at the same range of frequencies for all salt concentrations. Fig. 7 shows the calculated and experimental parallel displacement of the core particles as a function of frequency for different salt concentrations. In the calculations we assumed that the core particle had a surface potential of –50 mV for all three salt concentrations. Both the experiments and the finite-element calculations show similar parallel displacement as function of frequency. This is because the Debye lengths are much smaller than the inner shell diameter and the surface potential on the core and the shell are similar for all salt concentrations.

In this study, we did not experimentally investigate the mobility of core particles in pure water without added salt. However, in a previous collaboration between our groups it was observed that in pure water without added salt, core particles were confined to the middle of the yolk-shell geometry for a frequency of 1 kHz while hardly moving in the parallel direction [37]. This contrasts sharply with the driven motion from one end of the shell to the other, as observed at 1 kHz for the system with salt. To explain the difference, we calculated the parallel core displacement and maximum electrophoretic velocity for a core particle in 2  $\mu$ M salt ( $\kappa a_{\text{particle}} \approx 0.8$ ) and an electric-field strength of 100 V mm<sup>–1</sup>; all other parameters were kept the same as in the other calculations (Fig. 7b–c). Our results show that the parallel mobility of the core particle was indeed significantly reduced compared to the experiments in this work with higher ionic strength, which may explain why in the low-salt experiments no significant parallel, driven motion was observed at 1 kHz [37].

### 3.4. Influence of the inner shell diameter

Lastly, we investigated whether a larger shell would result in different frequency-dependent mobility patterns of the core particle. Fig. 8 shows experimental results for the mobility of a core particle ( $a_{\text{particle}} = 170$  nm) within two different shell sizes (inner radii  $a_{\text{shell}} = 370$  nm and  $a_{\text{shell}} = 496$  nm) and thicknesses ( $t_{\text{shell}} = 40$  nm and  $t_{\text{shell}} = 55$  nm). While the core particle moved parallel at

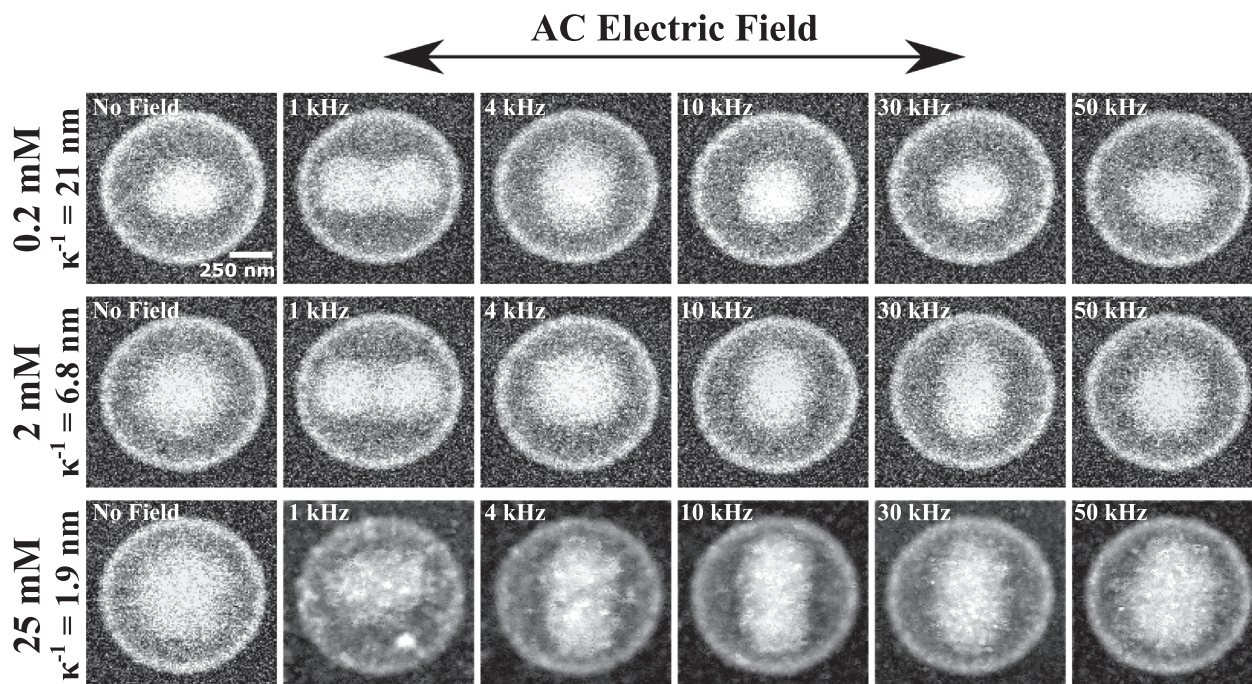


**Fig. 6.** Frequency-dependent displacement and mobility of a core particle within a shell under application of a  $100\text{Vmm}^{-1}$  AC electric field for various LiCl concentrations in water. The electron dose rate was  $45\text{e}^{-}\text{nm}^{-2}\text{s}^{-1}$ . The images here are cropped from the total movie that was 512 by 512 pixels, with a pixel size of 8.75 nm. The frame time was 1 s. The bright area within the shell indicates the part of the shell that was explored by the core over at least a 15 s period as observed in Supporting Movies 1, 4, and 5. The same trend is observed for all salt concentrations. While at lower frequencies the core moves parallel to the electric field, at intermediate frequencies the core moves orthogonal to the electric field. At high frequencies, there is no significant influence of the electric field. The images for 25 mM are cleared up for visibility due to contamination appearing in the sample, especially at low frequency electric fields, as seen in the image for 1 kHz.

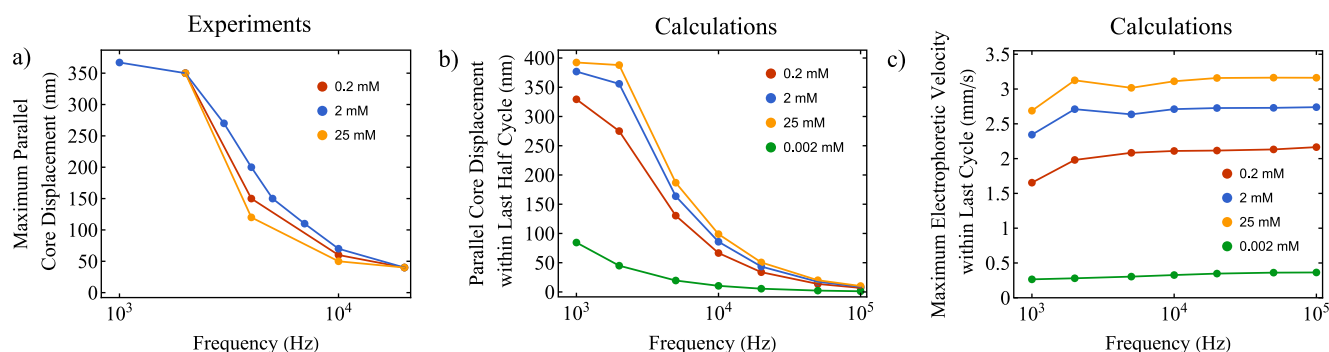


**Fig. 7.** Core particle mobility for different salt concentrations. a) The experimental maximum core displacement parallel to the electric field as obtained from Fig. 6 and Supporting Movies 1, 4 and 5. b) The calculated parallel displacement of the core within the last half cycle of the AC electric field for various salt concentrations as function of the frequency of the external AC electric field. c) The maximum electrophoretic velocity within the last cycle of the electric field. For all salt concentrations in the calculations, the core and shell had a surface potential of  $-50$  and  $-40\text{mV}$ , respectively. The shell was assumed to have a porosity of 10%.

2 kHz in the smaller shell, it was mostly confined to the middle in the larger shell for this frequency. At a lower frequency of 0.75 kHz, the mobility of the core within the larger shell was completely parallel, similar to the situation for the smaller shell. The transition from orthogonal motion to parallel motion was thus shifted to lower frequencies for a larger shell size. This is due to the longer path that the core particle has to travel in order to reach one side of the shell from the other for a bigger shell.

At a frequency of 10 kHz a particle in the smaller shell only moves diffusively in the direction orthogonal to the electric field, while a particle in the larger shell moves diffusively in all directions (best appreciated in Supporting Movie 6). For a frequency of 4 kHz, however, the particle in the larger shell is confined to only move diffusively in the direction orthogonal to the electric field.

The orthogonal motion regime shifting to lower frequencies for the larger shell is likely due to ionic gradients taking longer to be established, due to the larger shell size. This would be in line with our time-scale argument, as  $\tau_D$  changes from  $\tau_D \approx 1.0 \cdot 10^{-4}\text{s}$  for the small shell to  $\tau_D \approx 1.7 \cdot 10^{-3}\text{s}$  for the big shell.

In general, however, the quantitative parallel mobility of the core particles for different frequencies does not match up well with our calculations, even though the increased thickness of the shell was taken into account for the bigger shell (Fig. 8c-d). A likely explanation is that the porosity, which is taken the same as that of the small shell at 10%, is overestimated in our calculation for the larger shell. Such an overestimate would result in larger parallel motion for the core particle than observed in the experiments.



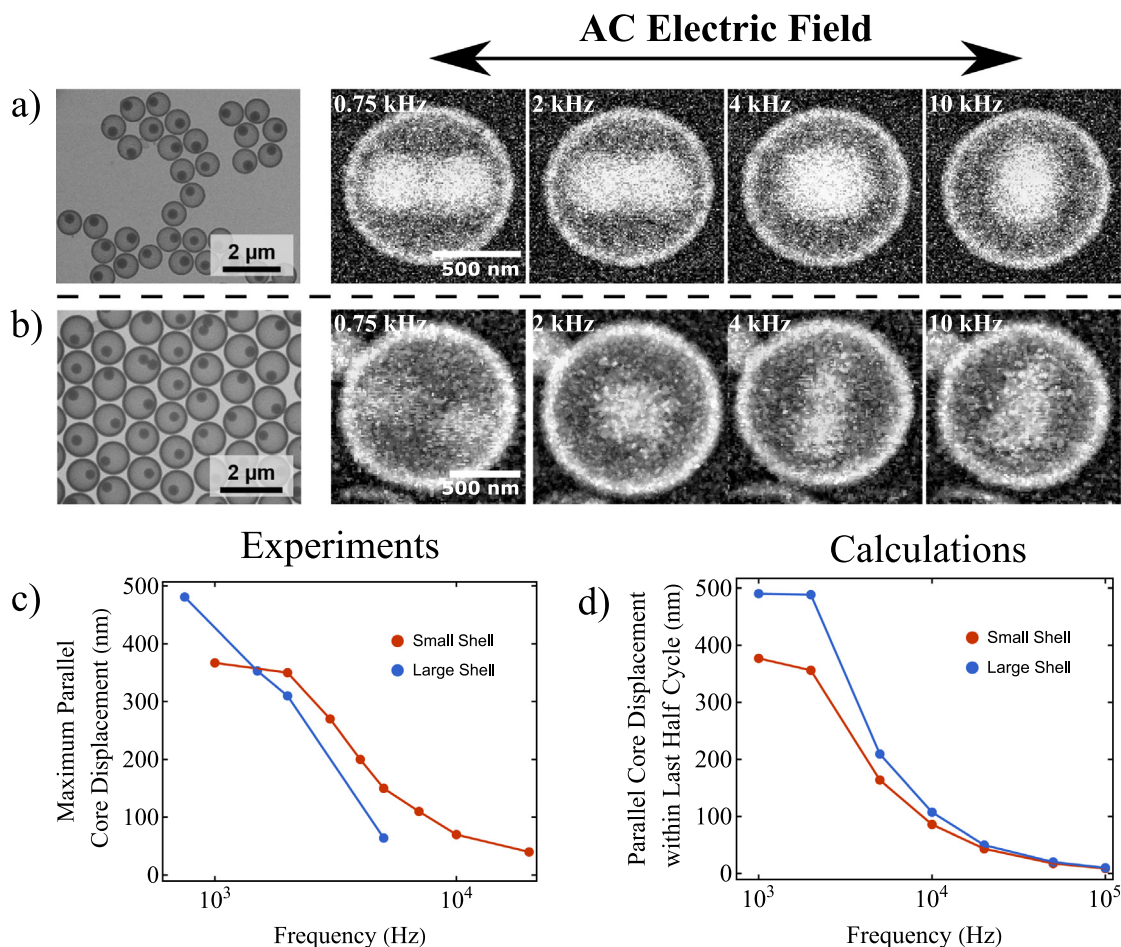


**Fig. 8.** a–b) Frequency-dependent mobility of a core particle ( $a_{\text{particle}} = 170 \text{ nm}$ ) within a shell under application of a  $100 \text{ V mm}^{-1}$  AC electric field for a small shell (inner radius  $a_{\text{shell}} = 370 \text{ nm}$ , shell thickness  $t_{\text{shell}} = 40 \text{ nm}$ ) and a bigger shell (inner radius  $a_{\text{shell}} = 496 \text{ nm}$ , shell thickness  $t_{\text{shell}} = 55 \text{ nm}$ ) in  $2 \text{ mM}$  (aq). For the smaller shell the electron dose rate was  $45 \text{ e}^{-} \text{ nm}^{-2} \text{ s}^{-1}$ . The images here are cropped from the total movie that was  $512$  by  $512$  pixels, with a pixel size of  $8.75 \text{ nm}$ . The frame time was  $1 \text{ s}$ . For the larger shell the electron dose rate was  $20 \text{ e}^{-} \text{ nm}^{-2} \text{ s}^{-1}$ . The images are cropped from the total movie that was  $512$  by  $512$  pixels, with a pixel size of  $12.2 \text{ nm}$ . The frame time was  $1 \text{ s}$ . The bright area within the shell indicates the part of the cavity that was explored by the core over at least a  $15 \text{ s}$  period as observed in Supporting Movies 1 and 6. c) Experimental parallel displacement of the core particles in small and big shells as function of frequencies. d) Parallel displacement of the core particle in the last half cycle of the electric field in finite-element calculations. The porosity of the shell in the calculations was  $10\%$  in both cases and the sizes of the cores and shells were taken the same as the experimental systems. For both the smaller and larger shell, the surface potential of the core was  $-50 \text{ mV}$  and the surface potential of the shell was  $-40 \text{ mV}$ .

#### 4. Conclusion

In summary, we studied the frequency-dependent mobility of a core particle within a shell subjected to an AC electric field. Building on previous experimental research [37], more types of motion exhibited by the cores were observed, which are recapped in Fig. 9. For a core ( $a_{\text{particle}} = 170 \text{ nm}$ ) in a shell ( $a_{\text{shell}} = 370 \text{ nm}$ ,  $t_{\text{shell}} = 40 \text{ nm}$ ) random motion of the cores was observed at high frequencies ( $> 40 \text{ kHz}$ ), predominantly orthogonal diffusive motion was observed at intermediate frequencies ( $3 - 40 \text{ kHz}$ ) and driven, parallel motion was found at low frequencies ( $< 3 \text{ kHz}$ ). We additionally expanded on earlier theoretical work [61,62,64] on the dynamic electrophoretic mobility of a particle in a cavity. Here, we allowed the particle to move in time according to the forces acting on it as obtained by solving the Poisson-Nernst-Planck-Stokes equations using a transient finite-element approach. We included in this an analysis of the influence of ion migration dynamics through the shell on the movement of the core. The orthogonal diffusive motion of the cores was shown to be due to the establishment of ionic gradients within the yolk-shell geometry limiting parallel excursions, while the parallel motion was directly driven by the electric field and was not diffusive. The porosity of the shell was found to significantly influence the core

motion within. A more porous shell led to the core particles being more confined to the middle of the shell for the frequencies that showed orthogonal, diffusive motion for the original shell. A thicker, less porous shell significantly decreased the frequency at which parallel, driven motion was observed and orthogonal motion was not observed at any frequency. We suspect that the primary cause of these differences is the reduction in the electric-field strength inside the yolk-shell geometry when the shell is made thicker and less porous.

A change of the LiCl concentration from  $0.2$ , to  $2$ , to  $25 \text{ mM}$  did not change the frequency-dependent motion patterns of the cores significantly in the experiments, as the double layers remained small compared to the particle size for all salt concentrations ( $\kappa a_{\text{particle}} \approx 8, 26, \text{ and } 88$ , respectively). This was confirmed by our finite-element calculations. Our model could also explain why experiments with the same yolk-shell particle in pure water that were done previously [37], did not show parallel, driven motion at  $1 \text{ kHz}$ . Lastly, the particles exhibited orthogonal diffusive motion at a lower frequency for a shell with a larger inner diameter, because it took longer to establish ionic concentration differences within a larger shell.

Despite Brownian motion not being included in the presented calculations, the main physical mechanisms were uncovered. The



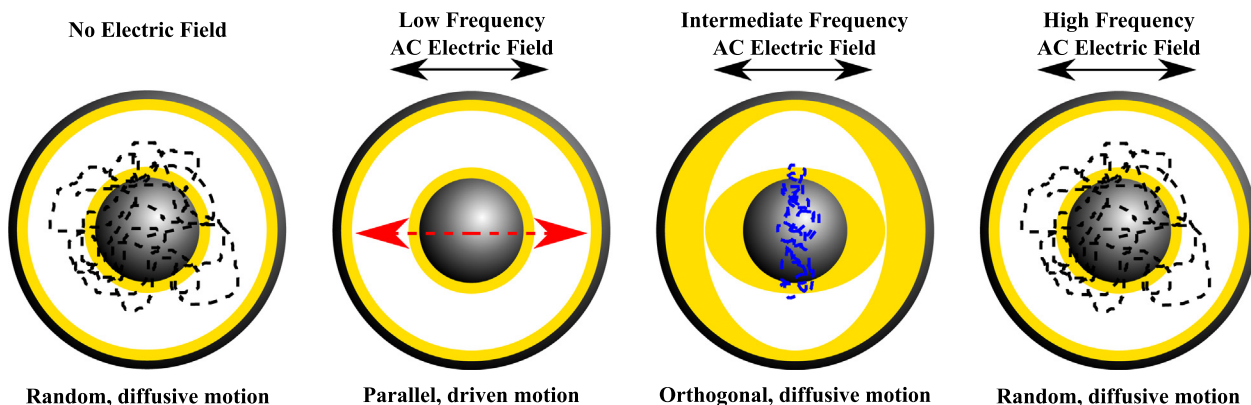


**Fig. 9.** Summary of electrodynamic regimes describing the observed mobility of the core particle within a yolk-shell geometry. When no electric field is applied, the core particle exhibits Brownian motion constricted by the double layers of the core and the shell. At lower frequencies compared to the relaxation time of the ions inside the liquid the core particle has enough time to move from one side of the shell to the other. At intermediate frequencies the ion distributions are significantly affected which results in orthogonal, diffusive motion and extended repulsions between cores and shells. At higher frequencies the electric field can influence the double layers slightly, but not sufficiently to change ionic concentrations within the whole shell geometry, which results in the particle exploring the same part of the shell diffusively as when no field was applied.

strong influence of ion migration through the shell on the electrophoretic mobility of the core particle highlights the importance understanding transport through thin porous layers in yolk-shell systems. We presume that this result will carry over to other systems involving encapsulation, such as vesicles. Further investigation and characterization of the porosity of the shell of these yolk-shell systems by employing electron tomography, physisorption, and differently sized ions is currently underway [74]. The combined insights obtained by experiment and numerical calculations into the complicated dynamics of this system of yolk-shell particles provides a roadmap to their future applications. For instance, we envisage that these yolk-shell particles are suitable building blocks for the creation of switchable photonic crystals, by employing the field-induced parallel motion of the core particles, or even their orthogonal motion.

## 5. CRediT authorship contribution statement

**Tom A.J. Welling:** Conceptualization, Methodology, Validation, Formal analysis, Investigation, Data Curation, Writing – Original Draft, Visualization. **Albert Grau-Carbonell:** Investigation. **Kanako Watanabe:** Conceptualization, Resources, Funding acquisition. **Daisuke Nagao:** Resources, Supervision, Funding acquisition. **Joost de Graaf:** Writing – Conceptualization, Review & Editing, Supervision, Funding acquisition. **Marijn A. van Huis:** Resources, Writing – Review & Editing, Supervision, Project administration, Funding acquisition. **Alfons van Blaaderen:** Conceptualization, Resources, Writing – Review & Editing, Supervision.

## Supplementary material

- Supporting Information for Publication: Additional details on finite-element calculations. Figure with details of mesh. Additional details on the shell overgrowth and etching. Figure of individual stills of experimental movies. Bright-field TEM images of used rattle-type particles. Figures on ionic concentrations and electric fields strengths in finite-element calculations.
- Movie S1: Experimental liquid-phase electron microscopy movie showing the mobility of a core particle within a yolk-shell geometry in 2 mM LiCl under AC electric field application of varying frequencies at  $100\text{Vmm}^{-1}$ . The arrow indicates the direction of the electric field. The electron dose rate was  $45\text{e}^{-}\text{nm}^{-2}\text{s}^{-1}$ .

- Movie S2: Experimental liquid-phase electron microscopy movie showing the mobility of a core particle within a yolk-shell geometry after additional etching in 2 mM LiCl under AC electric field application of varying frequencies at  $100\text{Vmm}^{-1}$ . The arrow indicates the direction of the electric field. The electron dose rate was  $148\text{e}^{-}\text{nm}^{-2}\text{s}^{-1}$ .
- Movie S3: Experimental liquid-phase electron microscopy movie showing the mobility of a core particle within a yolk-shell geometry (after shell overgrowth) in 2 mM LiCl under AC electric field application of varying frequencies at  $100\text{Vmm}^{-1}$ . The arrow indicates the direction of the electric field. The electron dose rate was  $148\text{e}^{-}\text{nm}^{-2}\text{s}^{-1}$ .
- Movie S4: Experimental liquid-phase electron microscopy movie showing the mobility of a core particle within a yolk-shell geometry in 0.2 mM LiCl under AC electric field application of varying frequencies at  $100\text{Vmm}^{-1}$ . The arrow indicates the direction of the electric field. The electron dose rate was  $45\text{e}^{-}\text{nm}^{-2}\text{s}^{-1}$ .
- Movie S5: Experimental liquid-phase electron microscopy movie showing the mobility of a core particle within a yolk-shell geometry in 25 mM LiCl under AC electric field application of varying frequencies at  $100\text{Vmm}^{-1}$ . The arrow indicates the direction of the electric field. The electron dose rate was  $45\text{e}^{-}\text{nm}^{-2}\text{s}^{-1}$ .
- Movie S6: Experimental liquid-phase electron microscopy movie showing the mobility of a core particle within a yolk-shell geometry with a large shell in 2 mM LiCl under AC electric field application of varying frequencies at  $100\text{Vmm}^{-1}$ . The arrow indicates the direction of the electric field. The electron dose rate was  $20\text{e}^{-}\text{nm}^{-2}\text{s}^{-1}$ .
- Movie S7: Calculated flow profile during the application of three cycles of the electric field as calculated via finite-element calculations for a yolk-shell geometry in 2 mM aqueous LiCl for an electric field with a strength of  $100\text{Vmm}^{-1}$  and frequencies of 50 and 2 kHz. The core particle has a surface potential of  $-50\text{mV}$ . The shell has a surface potential of  $-40\text{mV}$  and a porosity of 10%.
- Movie S8: Calculated total ion concentration profile during the application of three cycles of the electric field as calculated via finite-element calculations for a yolk-shell geometry in 2 mM aqueous LiCl for an electric field with a strength of  $100\text{Vmm}^{-1}$  and several frequencies ranging from 100 to 1 kHz. The core particle has a surface potential of  $-50\text{mV}$ . The shell has a surface potential of  $-40\text{mV}$  and a porosity of 10%.

- Movie S9: Calculated total ion concentration profile and mobility of the core when it is initially placed off-center during the application of three cycles of the electric field as calculated via finite-element calculations for a yolk-shell geometry in 2mM aqueous LiCl for an electric field with a strength of  $100\text{Vmm}^{-1}$  and 5kHz. The core particle has a surface potential of  $-50\text{mV}$ . The shell has a surface potential of  $-40\text{mV}$  and a porosity of 10%.

## Declaration of Competing Interest

The authors declare that they have no known competing financial interests or personal relationships that could have appeared to influence the work reported in this paper.

## Acknowledgment

This project has received funding from the European Research Council (ERC) via the ERC Consolidator Grant NANO-INSITU (Grant No. 683076). K. W. acknowledges funding from the Ministry of Education, Culture, Sports, Science and Technology, Japan (JSPS KAKENHI, Grant No. 21K14491). K. W. and D.N. acknowledge the support from the Ministry of Education, Culture, Sports, Science and Technology, Japan (Materials Processing Science project ("Materealize") of MEXT, Grant No. JPMXP0219192801). J. d. G. thanks NWO for funding through Start-Up Grant No. 740.018.013 and through association with the EU-FET Project No. NANOPHLOW (766972) within Horizon 2020.

## Appendix A. Supplementary material

Supplementary data associated with this article can be found, in the online version, at <https://doi.org/10.1016/j.jcis.2022.07.091>.

## References

- [1] J.F. Galisteo-López, M. Ibasate, R. Sapienza, L.S. Froufe-pérez, *Adv. Mater.* 23 (2011) 30–69.
- [2] X. Liu, Y. Zhang, D. Ge, J. Zhao, F. Endres, *PCCP* 14 (2012) 5100–5105.
- [3] V.L. Alexeev, S. Das, D.N. Finegold, S.A. Asher, *Clin. Chem.* 50 (2004) 2353–2360.
- [4] G.A. Ozin, K. Hou, B.V. Lotsch, L. Cademartini, D.P. Puzzo, F. Scotognella, A. Ghadimi, J. Thomson, *Mater. Today* 12 (2009) 12–23.
- [5] G. von Freymann, V. Kitaev, B.V. Lotsch, G.A. Ozin, *Chem. Soc. Rev.* 42 (2013) 2528–2554.
- [6] N. Vogel, M. Retsch, C.A. Fustin, A. Del Campo, U. Jonas, *Chem. Rev.* 115 (2015) 6265–6311.
- [7] Cai, Z.; Li, Z.; Ravaine, S.; He, M.; Song, Y.; Yin, Y.; Zheng, H.; Teng, J.; Zhang, A. From Colloidal Particles to Photonic Crystals: Advances in Self-Assembly and their Emerging Applications. 2021.
- [8] Z. Li, Y. Yin, *Adv. Mater.* 31 (2019) 1807061.
- [9] R.B. Wehrspohn, J. Üpping, *J. Opt.* 14 (2012) 24003.
- [10] L. Zhao, H. Liu, F. Wang, L. Zeng, *Journal of Materials Chemistry A* 2 (2014) 7065–7074.
- [11] Y. Yue, J.P. Gong, *J. Photochem. Photobiol., C* 23 (2015) 45–67.
- [12] Y. Takeoka, *Polym. J.* 47 (2015) 106–113.
- [13] S. Gaponenko, H.V. Demir, C. Seassal, U. Woggon, *Opt. Express* 24 (2016) A430–A433.
- [14] H. Inan, M. Poyraz, F. Inci, M.A. Lifson, M. Baday, B.T. Cunningham, U. Demirci, *Chem. Soc. Rev.* 46 (2017) 366–388.
- [15] J. Hou, M. Li, Y. Song, *Nano Today* 22 (2018) 132–144.
- [16] E.S. Goerlitz, R.N. Klupp Taylor, N. Vogel, *Bioinspired Photonic Pigments from Colloidal Self-Assembly*. (2018).
- [17] J.-T. Zhang, L. Wang, D.N. Lamont, S.S. Velankar, S.A. Asher, *Angewandte Chemie - International Edition* 51 (2012) 6117–6120.
- [18] A.C. Sharma, T. Jana, R. Kesavamoorthy, L. Shi, M.A. Virji, D.N. Finegold, S.A. Asher, *J. Am. Chem. Soc.* 126 (2004) 2971–2977.
- [19] B.I. Lee, D. Kim, J. Kal, H. Baek, D. Kwak, D. Go, *Adv. Mater.* 22 (2010) 4973–4977.
- [20] J. Ge, H. Lee, L. He, J. Kim, Z. Lu, H. Kim, J. Goebel, S. Kwon, Y. Yin, *J. Am. Chem. Soc.* 131 (2009) 15687–15694.
- [21] J. Ge, Y. Yin, *Journal of Material Chemistry* 20 (2010) 5777–5784.
- [22] L. He, M. Wang, J. Ge, Y. Yin, *Acc. Chem. Res.* 45 (2012) 1431–1440.
- [23] J.M. Weissman, H.B. Sunkara, A.S. Tse, S.A. Asher, *Science* 274 (1996) 959–960.
- [24] Y. Takeoka, M. Watanabe, *Langmuir* 19 (2003) 9104–9106.
- [25] P. Tierno, *PCCP* 16 (2014) 23515–23528.
- [26] D. Scheid, G. Cherkashinin, E. Ionescu, M. Gallei, *Langmuir* 30 (2014) 1204–1209.
- [27] S.K. Smoukov, S. Gangwal, M. Marquez, O.D. Velev, *Soft Matter* 5 (2009) 1285–1292.
- [28] S.H. Lee, C.M. Liddell, *Small* 5 (2009) 1957–1962.
- [29] S. Sacanna, L. Rossi, D.J. Pine, *J. Am. Chem. Soc.* 134 (2012) 6112–6115.
- [30] M.E. Leunissen, H.R. Vutukuri, A. van Blaaderen, *Adv. Mater.* 21 (2009) 3116–3120.
- [31] H.R. Vutukuri, F. Smalenburg, S. Badaire, A. Imhof, M. Dijkstra, A. van Blaaderen, *Soft Matter* 10 (2014) 9110–9119.
- [32] H.R. Vutukuri, S. Badaire, D.A. de Winter, A. Imhof, A. van Blaaderen, *Nano Lett.* 15 (2015) 5617–5623.
- [33] A.F. Demirörs, P.M. Johnson, C.M. van Kats, A. van Blaaderen, A. Imhof, *Langmuir* 26 (2010) 14466–14471.
- [34] D. Nagao, C.M. van Kats, K. Hayasaka, M. Sugimoto, M. Konno, A. Imhof, A. van Blaaderen, *Langmuir* 26 (2010) 5208–5212.
- [35] A. Okada, D. Nagao, T. Ueno, H. Ishii, M. Konno, *Langmuir* 29 (2013) 9004–9009.
- [36] K. Watanabe, D. Nagao, H. Ishii, M. Konno, *Langmuir* 31 (2015) 5306–5310.
- [37] K. Watanabe, H. Ishii, M. Konno, A. Imhof, A. van Blaaderen, D. Nagao, *Langmuir* 33 (2017) 296–302.
- [38] K. Watanabe, T.A.J. Welling, S. Sadighikia, H. Ishii, A. Imhof, M.A. van Huis, A. van Blaaderen, D. Nagao, *J. Colloid Interface Sci.* 566 (2020) 202–210.
- [39] A. van Blaaderen, M. Dijkstra, R. van Roij, A. Imhof, M. Kamp, B.W. Kwaadgras, T. Vissers, B. Liu, *European Physical Journal: Special Topics* 222 (2013) 2895–2909.
- [40] T.A.J. Welling, S. Sadighikia, K. Watanabe, A. Grau-Carbonell, M. Bransen, D. Nagao, A. van Blaaderen, M.A. van Huis, *Particle & Particle Systems Characterization* 37 (2020) 2000003.
- [41] M.N. Yesibolati, K.I. Mortensen, H. Sun, A. Broström, S. Tidemand-Lichtenberg, K. Mølhave, *Nano Lett.* 20 (2020) 7108–7115.
- [42] T.A.J. Welling, K. Watanabe, A. Grau-Carbonell, J. de Graaf, D. Nagao, A. Imhof, M.A. van Huis, A. van Blaaderen, *ACS Nano* 15 (2021) 11137–11149.
- [43] N. de Jonge, *Ultramicroscopy* 187 (2018) 113–125.
- [44] J. Overbeek, *Kolloid-Beihfte* (1943) 54.
- [45] H. Ohshima, *Reference Module in Chemistry, Molecular Sciences and Chemical Engineering*, Elsevier, 2016.
- [46] Delgado (ed), A. V. *Interfacial Electrokinesis and Electrophoresis* (1st ed.); CRC Press, 2002.
- [47] R.J. Hunter, *Zeta Potential in Colloid Science*, Academic Press, New York, 1981.
- [48] Hunter, R. J. *Foundations of Colloid Science*, Volumes I and II; Clarendon Press: Oxford, 1991.
- [49] W.B. Russel, D.A. Saville, W. Schowalter, *Colloidal Dispersions*, Cambridge University Press, Cambridge, 1989.
- [50] von Smoluchowski, M. In *Handbuch der Elektrizität und des Magnetismus*; Greatz, E., Ed.; 1921; pp 366–428.
- [51] E. Hückel, *Phys. Z.* 25 (1924) 204–210.
- [52] V.N. Shilov, A.V. Delgado, F. González-Caballero, J. Horno, J.J. López-García, C. Grosse, *J. Colloid Interface Sci.* 232 (2000) 141–148.
- [53] E. Lee, *Interface Science and Technology* 26 (2019) 123–142.
- [54] S.E. Gibb, R.J. Hunter, *J. Colloid Interface Sci.* 224 (2000) 99–111.
- [55] D. Mizuno, Y. Kimura, R. Hayakawa, *Langmuir* 16 (2000) 9547–9554.
- [56] C.S. Mangelsdorf, L.R.J. White, *Chem. Soc. Faraday Trans. 88* (1992) 3567–3581.
- [57] H. Ohshima, *J. Colloid Interface Sci.* 232 (1996) 431–438.
- [58] Zydney, A. L. *Boundary Effects on the Electrophoretic Motion of a Charged Particle in a Spherical Cavity*. 1995.
- [59] E. Lee, J.-W. Chu, J.P. Hsu, *J. Colloid Interface Sci.* 205 (1998) 65–76.
- [60] J.W. Chu, W.H. Lin, E. Lee, J.P. Hsu, *Langmuir* 17 (2001) 6289–6297.
- [61] C.P. Tung, E. Lee, J.P. Hsu, *J. Colloid Interface Sci.* 260 (2003) 118–125.
- [62] S.H. Lou, E. Lee, J.P. Hsu, *J. Colloid Interface Sci.* 285 (2005) 865–871.
- [63] E. Lee, W.L. Min, J.P. Hsu, *Langmuir* 22 (2006) 3920–3928.
- [64] J.P. Hsu, Z.S. Chen, M.H. Ku, L.H. Yeh, *J. Colloid Interface Sci.* 314 (2007) 256–263.
- [65] W.J. Chen, H.J. Keh, *J. Phys. Chem. B* 117 (2013) 9757–9767.
- [66] T.C. Lee, H.J. Keh, *European Journal of Mechanics, B/Fluids* 48 (2014) 183–192.
- [67] K. Tanaka, M. Nomura, *Journal of the Chemical Society, Faraday Transactions 1: Physical Chemistry in Condensed Phases* 83 (1987) 1779–1782.
- [68] A. van Blaaderen, J. Peetermans, G. Maret, J. Dhont, *J. Chem. Phys.* 96 (1992) 4591–4603.
- [69] R. Robinson, R. Stokes, *Electrolyte Solutions*, Butterworths, London, 1959.
- [70] D. Stein, M. Kruthof, C. Dekker, *Phys. Rev. Lett.* 93 (2004) 035901.
- [71] F. Fornasiero, H. Gyu, J.K. Holt, M. Stadermann, C.P. Grigoropoulos, A. Noy, O. Bakajin, *PNAS* 105 (2008) 17250–17255.
- [72] C. Aponte-Rivera, R.N. Zia, *Physical Review Fluids* 1 (2016) 023301.
- [73] A.E. Cervantes-Martínez, A. Ramírez-Saito, R. Armenta-Calderón, M.A. Ojeda-López, J.L. Arauz-Lara, *Physical Review E - Statistical, Nonlinear, and Soft Matter Physics* 83 (2011) 1–4.
- [74] K. Watanabe, T.A.J. Welling, Z. Peimanifard, R.G. Mendes, D. Nagao; A. van Blaaderen, to be submitted 2022.